Forces in Mechanics 6 (2022) 100067

Contents lists available at ScienceDirect

Forces in Mechanics

journal homepage: www.sciencedirect.com/journal/forces-in-mechanics

In-situ X-ray difraction analysis of reverted austenite in supermartensitic stainless steel weld deposits

S. Zappa [a,b,*], J.J. Hoyos [c], L. Tufaro [d], H. Svoboda [b,c]

[a] Facultad de Ingeniería, Universidad Nacional de Lomas de Zamora, Buenos Aires, Argentina
[b] Consejo Nacional de Investigaciones Científicas y Tecnológicas, CABA, Argentina
[c] Departamento de Ingeniería Mecánica, Facultad de Ingeniería, Universidad de Buenos Aires, Buenos Aires, Argentina
[d] Instituto Nacional de Tecnología Industrial, Buenos Aires, Argentina

ARTICLE INFO

Keywords:
Dilatometry
Critical temperatures
Synchrotron X-ray diffraction
Post weld heat treatment
Austenite stability

ABSTRACT

To improve the mechanical properties in supermartensitic stainless steel weld deposits, suitable post weld heat treatments (PWHT) are required, since these properties are controlled by the resulting microstructure. Some aspects of localized corrosion resistance could also be enhanced by the PWHT. In this sense, the austenite transformation or stability is a key issue. The aim of this work is to "*in-situ*" analyze the evolution of austenite during the thermal cycle associated to a post weld inter-critical heat treatment in a supermartensitic stainless steel weld deposit, by means of a thermomechanical simulator integrated on a synchrotron X-ray diffraction line. An all-weld metal coupon was welded with a semi-automatic process. Dilatometry measurements were performed at different heating rates (1, 10 and 100 K/s) in the thermomechanical simulator, to determine the critical transformation temperatures ($Ac1$ and $Ac3$) of the all-weld metal. To study the phase transformation during the applied thermal cycle (heating to 938 K at 1 K/s, maintenance during 15 min and cooling to room temperature at 2 K/s), *in-situ* synchrotron X-ray diffraction measurements were carried out in the facilities of National Laboratory Synchrotron Light (Campinas, Brasil). The microstructural evolution was discussed in terms of volumetric phase fractions, micro-deformation and crystallite size. The techniques used allow to detect the critical transformation temperatures, phase transformations and their kinetics, monitoring particularly the austenite evolution during the post weld heat treatment cycle. At the inter-critical temperature 71% of austenite was formed, after the 8.5 min from the 15 min of permanence. Finally, at room temperature 29% of stable reverted austenite was obtained. Both martensite and austenite there did not show significant variations during the thermal cycle both for microstrain and crystallite size.

1. Introduction

Supermartensitic stainless steels (*SMSS*) were developed from classic martensitic stainless steels (11–14% Cr), reducing *C* content to enhance weldability and corrosion resistance and adding *Ni* to promote a ferrite-free structure and *Mo*, which also improves corrosion resistance [1]. In recent years, this steel has been widely used in flow lines for transporting unprocessed fluid in the oil and gas industry, replacing classic martensitic and duplex stainless steels, due to the appropriate combination of weldability, toughness, corrosion resistance and the ease of performing heat treatments, at a comparatively lower price [2,3]. Generally, these materials are an economical alternative against uncoated carbon steels, carbon steel used without inhibitors or duplex stainless steels in some environments [3]. Furthermore, their relatively lower cost makes them an attractive option as a substitute for more expensive duplex and superduplex stainless steels, and their use in offshore deep water tubing applications has significantly increased in the last years [4].

SMSS exhibit the following typical mechanical properties: 25–32 RC hardness, 650–750 MPa of 0.2% offset yield strength, 880–950 MPa tensile strength, elongation at rupture of up to 20%, and Charpy V-notched absorbed energy up to 100 J at room temperature (RT) [5]. These properties strongly depend on the microstructure, which is usually depending on the thermomechanical history and composition [6].

In the present alloy grade, delta ferrite is the first solidifying phase (1753–1733 K), which partially or completely transforms to austenite

* Corresponding author at: Facultad de Ingeniería, Universidad Nacional de Lomas de Zamora, Buenos Aires, Argentina.
E-mail address: zappasebastian@hotmail.com (S. Zappa).

https://doi.org/10.1016/j.finmec.2021.100067
Received 14 November 2021; Received in revised form 17 December 2021; Accepted 17 December 2021
Available online 20 December 2021

during cooling (1653–1453 K). The main austenite to martensite transformation occurs at lower temperatures (503–463 K) [7]. In this sentences, *SMSS* also consist of martensite and variable amount of austenite (up to 30%) and ferrite (up to 10%), with different morphologies [1]. The presence of the ferrite phase can cause severe reduction of toughness and ductility. Further, it can locally interrupt the passivation layer through *Cr*-depletion in martensite and formation of *Cr* carbides near ferrite, which leads to degradation of the corrosion resistance [8]. When retained, it is only possible to dissolve ferrite by extensive heat treatment, which is uneconomical and can lead to undesired grain growth [8].

The high toughness of the steel is usually achieved when the tempering temperature is close to austenite start temperature ($Ac1$), owing to the existence of amounts of finely distributed austenite along the martensite interlath boundaries and prior austenite grain boundaries [5,9,10]. Inappropriate heat treatment may cause important changes in microstructure and serious decrease in mechanical properties [9]. In this sense, the content of retained austenite gradually increases with intercritical temperature up to maximum value. As the intercritical temperature continues to rise, the content of retained austenite gradually decreases [6,9].

The austenite start ($Ac1$) and finish ($Ac3$) transformation temperatures strongly dependent on the heating rate. This fact could be relevant for welding or *PWHT* [7]. The critical temperature for onset the transformation of austenite into martensite during the cooling (Ms) is in the order of 403 K for *SMSS* weld deposits [11].

Post Weld Heat Treatment (*PWHT*) is usually recommended for welded joints of these steels for martensite tempering, thus improving the toughness and ductility. Because of the increased *Ni* content, the $Ac1$ temperature is usually lower than 873 K, and correspondingly lower than the typical tempering range for martensitic steels (923–1023 K). Tempering above the *As* will result in reformation of some austenite and subsequent formation of "fresh" martensite upon cooling.

The austenite formed during the heating and retained to RT is related to the additional alloying elements (*Ni* and *Mo*) [9]. The *PWHT* leads to formation of reverted austenite in a finely dispersed lamellar morphology on grain boundaries of lath martensite. These places present high defect density, which can provide the energy of austenite nucleation and the quick diffusion access for *Ni* [12]. This is accompanied by the segregation gammagene elements into austenite, which stabilize this phase at RT [8]. In this way, through a diffusional mechanism, the austenite produced during the tempering is enriched in elements such as *N*, *C* and *Ni*. This enrichment will determine the stability of austenite formed during the treatment. If tempering is carried out at temperatures slightly above $Ac1$, the enriched austenite will be stable at RT. On the other hand, if the treatment is performed at temperatures well above or well below $Ac1$, the austenite will lose chemical enrichment and, consequently, its stability. Thus, the martensitic transformation is easily induced owing to the decrease of thermal instability of austenite [12–14].

Since the good mechanical properties of the alloy depend on this stabilization of reverted austenite, it is vital to control the compositional homogeneity of the initial martensitic microstructure prior to tempering [8].

There are three main mechanisms for the generation of nanometric size reverted austenite [15]:

1 Generation of allotriomorphic austenite (with irregular faces) coherent at the interface (with K-S orientation), located between martensite lath, aided by a strong segregation of gammagene elements.
2 Growth of a previously existing retained or reverted austenite.
3 Austenite nucleation aided by the precipitation of carbides that act as heterogeneous nucleation sites.

In this sense, the austenite generation mechanism more accepted in the literature is mainly associated with the segregation of austenite stabilizing elements at the edges between martensite lath, followed by austenite nucleation and growth, mainly controlled by the local equilibrium partition of *Ni* at the tempering temperature [15].

The reverted austenite will not transform into martensite even at very low temperatures. However, once plastic deformation occurs, the reverted austenite will absorb the deformation work and transform to martensite partially. Thereby, the plasticity and toughness of material at low temperatures can be enhanced [12].

The remaining high content of reverted austenite has shown beneficial effects. Tavares et al. [16] reported an increase of toughness with tempering treatments, due to the increase of reverted austenite and to the associated TRIP effect. Also, Man et al. [17] confirmed that the reverted austenite had a beneficial effect on the intergranular corrosion of the martensitic stainless steel. Firstly, the formation of reverted austenite at the Cr-depleted regions reduced the number of nucleation sites for intergranular corrosion. Secondly, the reverted austenite was always distributed along the martensite lath boundaries, which prevented the propagation of intergranular corrosion.

The comprehension of the mechanisms and the kinetics of reverted austenite formation and its stability at RT is still not clear, particularly for weld metals, where segregation and retained austenite could affect them.

The aim of this work is to analyze "*in-situ*" the evolution of austenite during the heating, maintenance and cooling in post weld inter-critical heat treatment in a *SMSS* weld deposit, by means of a thermomechanical simulator (*TMS*) integrated on a Synchrotron X-Ray Diffraction ($S-XRD$) line.

2. Experimental procedure

2.1. Materials

An all-weld metal (*AWM*) coupon was welded according to the AWS A5.22 standard [18]. Metal Cored Arc Welding (*MCAW*) process was employed, with a *SMSS* tubular filler wire of 1.2 mm in diameter, using an $Ar + 5\%$ *He* gas protection, with a flow rate of 18 L/min. The welding was performed in flat position, the electrode to piece distance was approximately 20 mm, and preheat and inter-pass temperatures were 373 K. Table 1 shows the welding parameters used.

Fig. 1 shows a cross section a macrograph of the weld deposit in As Welded (*AW*) condition, where different zones can be identified: base metal (*BM*) plates, buttered area and the central area of *AWM* zone. Transversal specimens for dilatometry and phase transformations studies were extracted centered on the *AWM* zone, according to the scheme of the Fig. 1. Their thickness was 2 mm. This zone is free from dilution with the *BM*, so that the chemical composition is associated to the filler material. To assure the position of the sample, electrical discharge machining (*EDM*) wire cutting was used with a 0.2 mm diameter *Mo* wire.

The chemical composition at the *AWM* zone was determined by optical emission spectrometry, except for the *C*, *O*, *N* and *S* contents that were measured by combustion techniques. Initial microstructure and phases quantification were also analyzed by means of scanning electron microscopy (*SEM*) and X-Ray Diffraction (*XRD*). In the case of SEM images, quantitative metallography was done to determine the ferrite content using an image analysis software.

Table 1
Welding parameters.

Tension	Current	Weld. Speed	Heat input
[V]	[A]	[mm/s]	[kJ/mm]
29	298	5	1.7

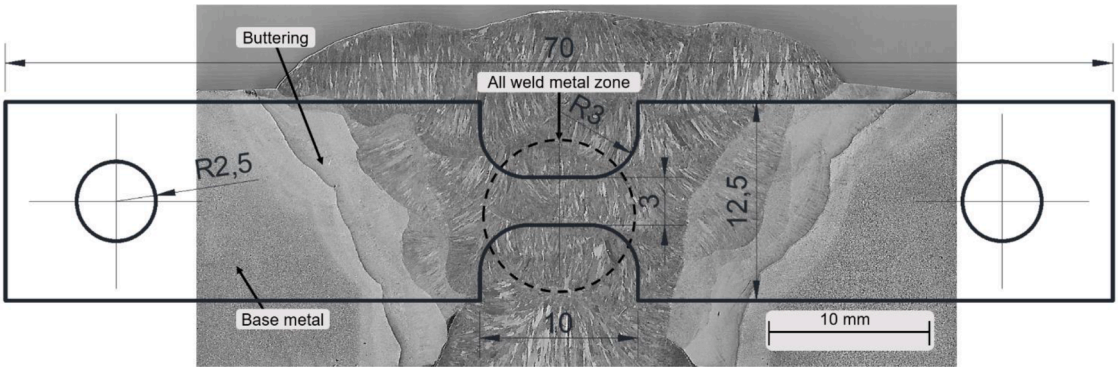

Fig. 1. *AWM* deposit of *SMSS* and dimensions of the extracted specimens used for dilatometry and phase transformations studies.

2.2. Dilatometry

Dilatometry tests were carried out to determine the *Ac*1 and *Ac*3 temperatures at three different heating rates (*HR*) according to Table 2.

Samples shown in Fig. 1 were used. A type K thermocouple was welded at the center of the calibrated length of the sample. These tests were carried out at a Gleeble 3S50 instrumented with a laser dilatometer, under a vacuum atmosphere (10^{-1} Pa), which measures the change in cross section. For each case, dilatation, temperature and time were recorded during the applied thermal cycle, obtaining curves dilation vs temperature, from which *Ac*1, *Ac*3 and *Ms* temperatures were determined.

2.3. In-situ synchrotron X-ray diffraction (S-XRD) study

The *Ac*1 and *Ac*3 temperatures, experimentally determined by dilatometry, were used to define the *PWHT* temperature at 938 K. Such intercritical tempering temperature was established as *Ac*1 + 40 K, since the highest reverted austenite contents are reached at this temperature [2]. For this condition, the heating and cooling rates were defined at 1 and 2 K/s, respectively.

To study austenite transformation kinetics during the intercritical *PWHT* (heating, holding and cooling) *in-situ S − XRD* measurements were carried out at 1 K/s. The experiments were performed using a Synchrotron beam with an energy of 12 keV and a wavelength of 0.10332 nm. The diffracted intensity was measured using two solid state linear detectors Mythen (1080 pixels each one), which simultaneously measured a 20° angular region around the center of the specimen. It was placed in a fixed position and inclined at 15° in relation to the incident beam. The obtained data during the different stages of the *PWHT*, were recorded continuously in a 2θ range of 28 to 49°, identifying the austenite peaks corresponding to planes {111}, {200} and {220} and martensite / ferrite {110} and {200}, with an acquisition time of 3.15 s. This means that every 3.15 s, a *XRD* spectrum with information about the microstructural evolution during heating, holding and cooling is obtained. In addition, to get a more detailed information, complete scans in a 2θ range from 28 to 88°, with a scan time of 210 s, were performed in constant temperature stages.

From the *XRD* spectra measured, the volume fractions x_i of the particular phases were estimated from the integrated intensity I_i and the theoretical intensity R_i of each diffraction peak, according to Eqs. (1)–(3), respectively [19,20].

$$x_i = \frac{\frac{1}{N}\sum_{j=1}^{N}\left(\frac{I_{i,j}^{hkl}}{R_{i,j}^{hkl}}\right)}{\sum_i\left(\frac{1}{N}\right)\sum_{j=1}^{N}\left(\frac{I_{i,j}^{hkl}}{R_{i,j}^{hkl}}\right)} \tag{1}$$

$$R^{hkl} = \frac{\rho^{hkl}\left|F^{hkl}\right|^2\left(e-\left(1+\frac{sin\omega}{\sin(2\theta-\omega)}+2M(\theta)\right)\right)}{v_i^2(4sin^2\theta cos\theta)} \tag{2}$$

$$M(\theta) = \frac{6\ h^2\ T}{m\ k\ \Phi^2}\left(\varphi(x)+\frac{x}{4}\right)\left(\frac{\sin(\theta)}{\lambda}\right)^2 \tag{3}$$

Where ρ^{hkl} is the plane multiplicity factor, F^{hkl} is the plane structure factor, v_i is the volume of the unit cell, θ the Bragg angle, ω the angle of incident beam (around 15°), $M(\theta)$ the Debye-Waller factor, h the Planck's constant (6.63 × 10–34 m^2Kg/s), T the absolute temperature, m the mass of the vibrating atom, k the Boltzmann's constant (1.38 × 10^{-23} $m^2Kgs^{-2}K^{-1}$), Φ the Debye characteristic temperature of steel, x the ration between the Debye and steel temperatures, λ the wavelength in angstroms (1.033 Angstroms), $\varphi(x)$ the Debye function.

The average crystallite size and lattice microstrain of each phase were estimated using the Williamson – Hall method [21,22], according to Eq. (4). In this method, the spectra obtained from scans were analyzed (*AW* at 298 K, Holding at 938 K and *PWHT* at RT). For martensite, the families of planes {110}; {200}; {211}; {220}; {222}; {321} were used. On the other hand, for austenite, the families of planes {111}; {200}; {220}; {311}; {222}; {331}; {420} were used.

$$\frac{(\beta\ cos\theta)}{\lambda} = \left(\frac{1}{D}\right) + 4\ \eta\left(\frac{sin\theta}{\lambda}\right) \tag{4}$$

Where D is the crystallite size, η the lattice microstrain, and β is the corrected Full Width at Half Maximum (*FWHM*). The D and η were respectively obtained from the intercept and the slope of $\beta\ cos\theta\ /\ \lambda$ plotted against $4\ sin\theta\ /\ \lambda$. The instrument broadening was calculated according to Caglioti equation (Eq. (5)) [20,21], using the parameters reported by Carvalho et al. [20].

$$FWHM = \left(0.004289\ \tan^2\theta + 0.000548\ \tan\theta + 0.001102\ \right)^{1/2} \tag{5}$$

Nevertheless, the crystallite size of the austenite is not reported since the values are negative, and consequently, do not have physical meaning [21]. The average crystallite size (D) of each phase was estimated from the Scherrer Equation, according to Eq. (6). It is worth noting that this equation led to an underestimation of the Crystallite Size because it does not consider the effects of the lattice strain in the peak broadening.

$$D = \left(\frac{\lambda}{\beta cos\theta}\right) \tag{6}$$

Table 2
Parameters of dilatometry tests.

Heating Rate	Max. Temperature	Holding Time	Cooling rate
[K/s]	[K]	[s]	[K/s]
1	1273	60	20
10	1273	60	20
100	1273	60	20

Fig. 2. A shows an image corresponding to the Gleeble 3S50 equipment linked to the X-ray diffraction line and Fig. 1.B shows the imposed intercritical treatment cycle.

3. Results and discussion

3.1. Chemical composition

Table 3 shows the chemical composition measured from the *SMSS* AWM. The obtained values are according with the specified for this material [13]. *O* and *N* contents are also in values usually observed.

Transformation temperatures are mainly dependent on chemical composition, among other factors. In martensitic stainless steel with high *Ni* content, *Ac*1 can be around 823 K [23]. In the literature there were proposed different equations to estimate *Ac*1 (Eq. (7), in °C) and *Ms* Eq. (8)) [13,23,24].

$$Ac1 = 850 - 1500(C+N) - 50Ni - 25Mn + 25Si + 25Mo + 20(Cr - 10) \quad (7)$$

$$Ms = 540 - 497C - 6.3Mn - 36.3Ni - 10Cr - 46.6Mo \quad (8)$$

According to Eqs. (7) and (8), *Ac*1 temperature should be 861 K and the *Ms* temperature 322 K, respectively, considering the chemical composition of the AWM showed in Table 2. However, these equations are for reference only, since they do not consider heating or cooling rates, etc.

3.2. Dilatometry

Fig. 3 shows the obtained dilatometry curves for the different heating rates, in as measured condition and filtered. From these curves, *Ac*1 and *Ac*3, were obtained. Furthermore, *Ms* was also determined. Additionally, it can be seen that the *Mf* (final transformation temperature of austenite into martensite) was not reached, because it is under RT. Table 4 shows the values of critical temperatures determined.

*Ac*1 and *Ac*3 showed dependence with the heating rate in the analyzed welded deposit, as it was previously reported for other materials [25]. Both temperatures increased as *HR* increased from 1 to 100 K/s. Af was a less sensible to *HR*. The characteristic transformation temperatures are shifted to higher temperatures with increasing heating rate, which is a well-known effect due to the thermally activated character of the transformation [26]. The range of transformation of martensite into austenite (*Ac*3 - *Ac*1) decreases as the *HR* increases.

These results show the importance of controlling the *HR* during the application of heat treatments, especially in those materials that have a narrow range of critical temperatures, such as supermartensitic stainless steel [7,23]. In this case *Ac*1, *Ac*3 and Ms temperatures were significantly higher than the value estimated by Eqs. (7) and (8), probably associated to the extra low carbon content of this material, compared with the conventional martensitic stainless steels.

As it was mentioned before, from the *Ac*1 measured values it was define the intercritical temperature for the PWHT in 938 K, in order to maximize the reverted austenite formation.

3.3. In-situ monitoring of phase transformation during PWHT cycle

Stage 1: As welded condition

Fig. 4 shows the microstructure and the present phases in *SMSS AWM* in *AW* condition. Martensite with a low content of ferrite can be observed in the Fig. 4.A, usually obtained in SMSS weld metals [11]. Also, peaks corresponding to austenite and martensite/ferrite can be identified in the *XRD* pattern of the Fig. 4.B.

The microstructure in *AW* condition was composed by a predominantly martensitic matrix, with the presence of 9% delta ferrite (in its different morphologies) and 5% retained austenite. The presence of ferrite and austenite is due to the incomplete transformation into austenite and martensite, respectively, during cooling in solid state. As mentioned above, the ferrite and retained austenite content, affects the final mechanical properties in opposite directions. A higher content of ferrite decreases the toughness of the weld deposits, while retained austenite increases and ductility [13].

Stage 2: Heating at 1 K/s to 938 K

Fig. 5 shows the evolution of the main austenite peak {111} during heating. A shift of all austenite and martensite peaks towards lower angles can be observed, associated with phase dilation and the increase in the inter-planar distance generated by temperature [27]. In this sense, the shift of austenite is greater than that of martensite, due to the higher linear expansion coefficient of the austenite [28]. In addition, from 894 K the growth of the austenite peaks and the decrease of the martensite ones were observed. This evolution corresponds to the transformation of martensite into austenite, thus identifying the lower critical transformation temperature *Ac*1.

It is known for the *SMSS* steel that *Ni* is crucial for stabilizing the austenite at RT, because austenite is enriched in *Ni* during heating and maintaining. Since *Ni* lowers the temperature range over which austenite is stable in the 13Cr6Ni2Mo *SMSS*, *Ni* rich zones are transformed first to austenite during heating, followed by *Ni* depleted zones. The *Ni* rich regions transform to austenite first, due to their lower *Ac*1 temperature [28]. In this sense, other authors [29] report that a higher rate of transformation of martensite into austenite is achieved for *SMSS* steels with higher *Ni* contents. The *Ac*1 detected are in good agreement with the value obtained previously by dilatometry (898 K).

Stage 3: Holding at 938 K for 900 s

Fig. 6.A shows the superposition of various diffraction patterns during the first 11.5 min of permanence at 939 K.

Once the intercritical tempering temperature is reached, austenite grows rapidly during the first 514 s (8.5 min). After this time, the austenite content remains constant until the end of the tempering time. Fig. 6.B shows the complete *XRD* pattern of the scan at the end of this stage. At this time, the austenite content was approximately 71%.

Other authors have reported studies of transformation of martensite into austenite at constant temperature for SMSS [26]. In dilatometry tests, the change in relative length during holding is greater for higher heating rates. These observations again imply the process being

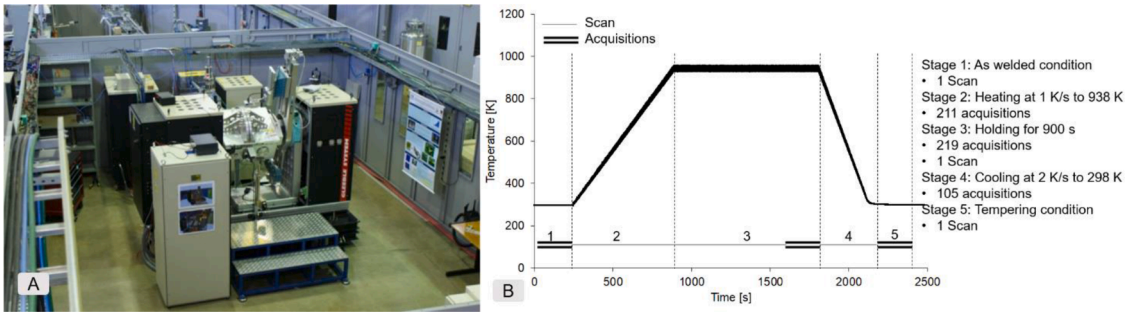

Fig. 2. A: Gleeble 3S50 equipment linked to the X-ray diffraction line; B: intercritical treatment cycle.

Table 3
Chemical composition of the weld deposit.

C	Mn	Si	S	P	Cr	Ni	Mo	Cu	V	Nb	O	N
[%wt]	[%wt]	[%wt]	[%wt]	[%wt]	[%wt]	[%wt]	[%wt]	[%wt]	[%wt]	[%wt]	[ppm]	[ppm]
0.012	1.76	0.44	0.013	0.015	12.13	6.27	2.69	0.49	0.09	0.01	390	50

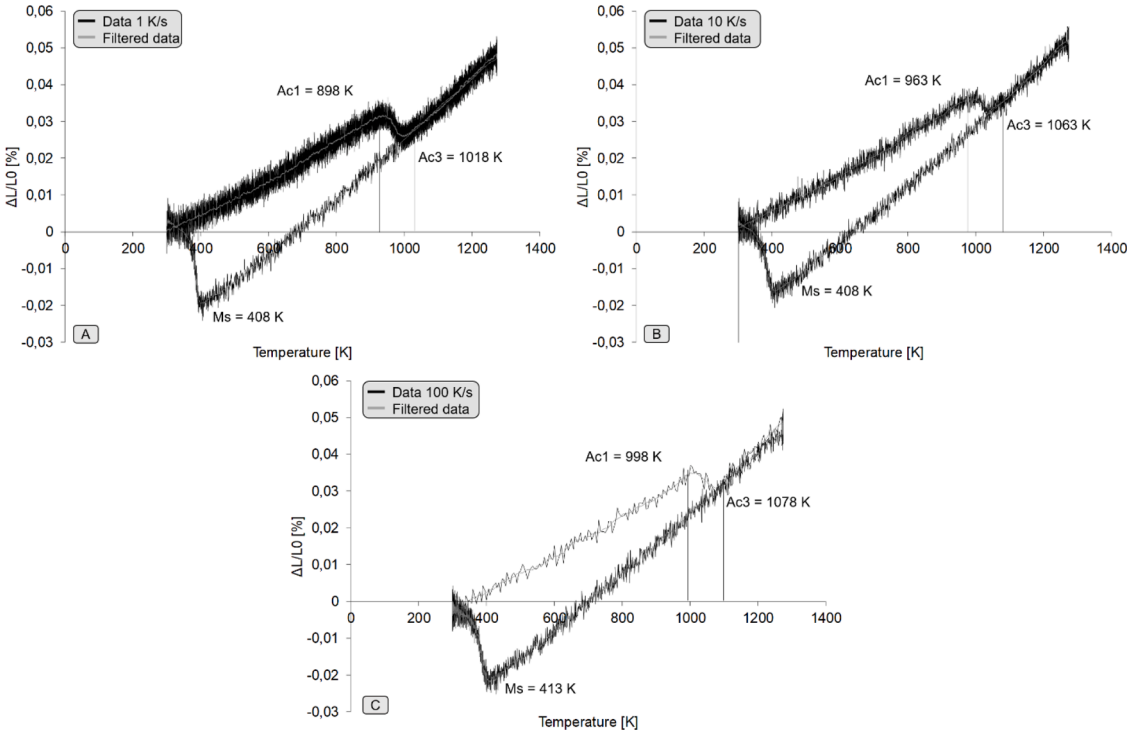

Fig. 3. Dilatometry curves for different heating rates. Measured and Filtered data.

Table 4
Critical temperatures determined by dilatometry.

HR	*Ac*1	*Ac*3	*Ac*3 - *Ac*1	*Ms*
[K/s]	[K]	[K]	[K]	[K]
1	898	1018	393	408
10	963	1063	373	408
100	998	1078	353	413

diffusional [26].

Stage 4: Cooling at 2 K/s to RT

Fig. 7 shows the overlap of various diffraction patterns as it was cooled from 938 K to RT. A shift of all austenite and martensite peaks towards higher angles can be observed, associated with contraction phenomena of the phases and the decrease in the interplanar distance generated by temperature [27].

Starting at 423 K, a decrease in austenite peaks and an increase in martensite peaks were observed. This evolution corresponds to the transformation of austenite into martensite *Ms*, showing a good agreement with the results obtained by dilatometry.

Stage 5: Tempering condition

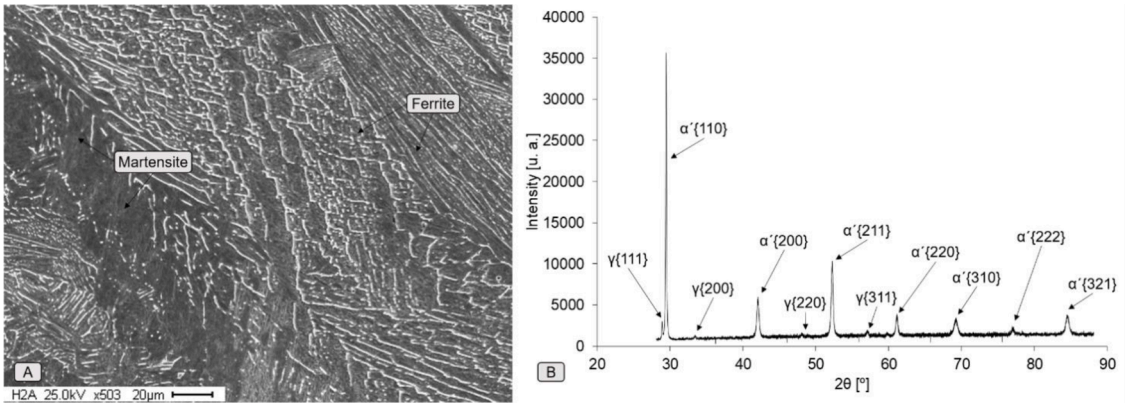

Fig. 4. AW condition. A. Microstructure (*SEM*); B: *XRD* pattern showing alpha/alpha' and gamma diffraction peaks in *AW*.

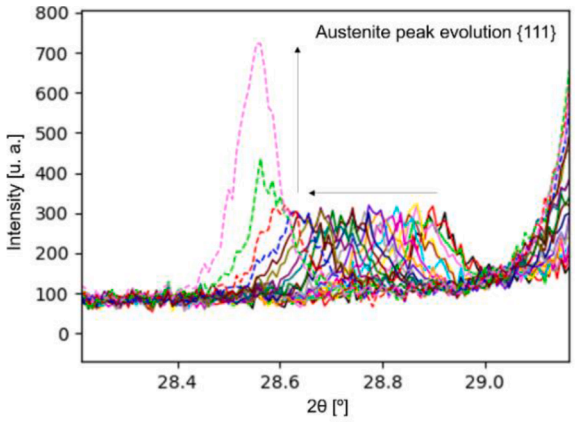

Fig. 5. Shift and growth of the main austenite peak {111} during heating.

Fig. 8.A shows a SEM image and Fig. 8B the XRD pattern of the *SMSS* all-weld metal in the final PWHT condition.

The resulting microstructure is composed by a martensitic matrix with a low ferrite content in its different morphologies, since tempering does not alter this phase, and reverted austenite.

Fig. 9.A shows the intensity map, while Fig. 9.B the evolution of the austenite transformation during the whole thermal cycle studied. An intensity map is a graph that relates the diffraction angle 2θ, the test time and the intensities of the diffraction spectrum (by the intensity of the color), where the red color corresponds to the position of the highest intensity peaks and green the least.

Austenite starts to form at 894 K. Once the tempering temperature is reached, the austenite content continues increasing (for 8.5 min) up to 71%. During cooling, below 423 K, austenite begins to transform into a martensite.

The mechanism that explains the stability of reverted austenite at RT is associated with chemical and morphological issues [26,28,30,31]. During heating in the PWHT, before reaching the temperature *Ac*1, the progressive segregation of *Ni*, *Mn*, *C* and *N* take place, mainly at the grain boundary. Also, said segregation of elements generates a change in the volume of the elemental cell of martensite [32]. However, this phenomenon does not participate in the generation of austenite [15]. Once the *Ac*1 temperature is reached, the austenite content grows, enriching itself in gammagene elements (mainly *Ni* and *Mn*), as mentioned above. The stability of the austenite particles depends on the intercritical tempering temperature, which defines the enrichment level (more enrichment of *Ni* for low intercritical temperatures). Austenite particles with more than 8% *Ni* in solution will be retained after cooling [31].

Fig. 10 shows schematics describing the microstructural evolution during the different stages of the PWHT analyzed in the present work: Stage 1: As welded condition at RT; Stage 3: End of holding at 938 K for 900 s at 938 K; Stage 5: Tempering condition at RT.

In this stage, the estimated phases content was 20% tempered martensite (the martensite that did not transform into austenite during tempering), 9% ferrite (since intercritical tempering does not alter this phase), 29% of reverted austenite (the austenite that remained stable after cooling the tempering) and 42% of fresh martensite (that new martensite that produces from the transformation of austenite during the cooling to RT).

According to Escobar et al. [31], the stability of austenite is divided into three regions, depending on the temperature of the tempering heat treatment:

1 Total stability (temperatures close above *Ac*1).
2 Partial stability (temperatures between *Ac*1 and *Ac*3).
3 Instability (temperatures close to or above *Ac*3).

In this work, the heat treatment used corresponds to region 2, since not all the austenite generated at high temperature remained stable at RT. In this sense, during cooling part of the reverted austenite is transformed into fresh martensite (saturated in *C*). The stable reverted austenite and the recently created fresh martensite have the same morphology, but different chemical compositions [33].

3.4. Lattice microstrain and crystallite size

Fig. 11 shows the Williamson-Hall plots for the stages 1, 3 and 5 (scan patterns were used). The linear fitting allows estimating the lattice microstrain and crystallite size from the slop and the inverse of the intercept, respectively. Table 5 displays the values obtained for both

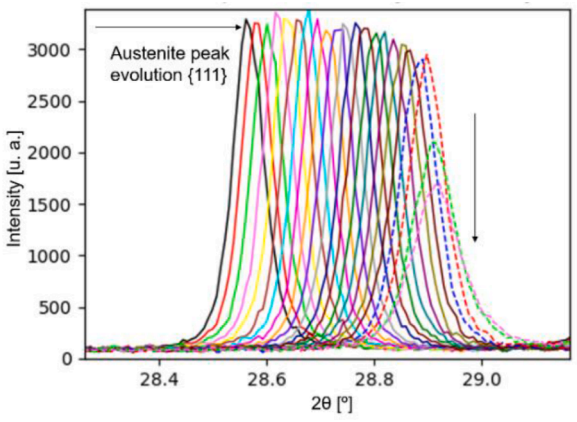

Fig. 7. Shift and decrease of the main austenite peak {111} during cooling.

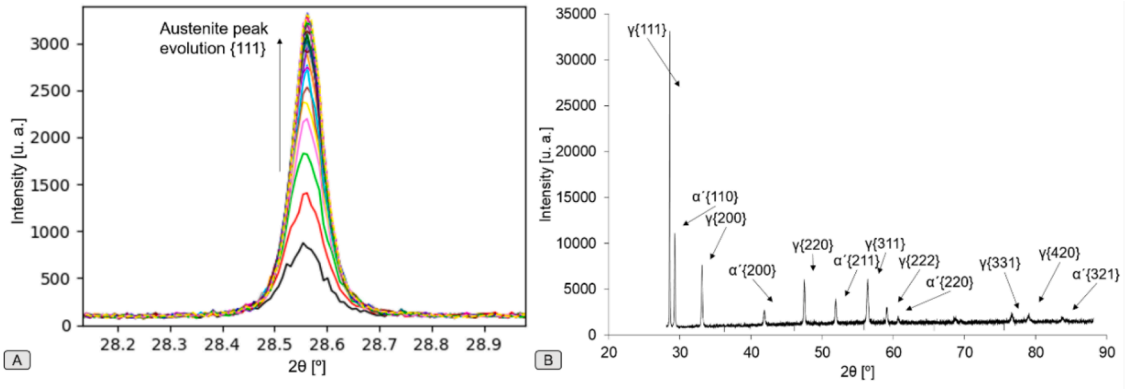

Fig. 6. A: Growth of the main austenite peak {111} during maintenance; B: *XRD* pattern showing alpha/alpha' and gamma diffraction peaks in holding at 938 K.

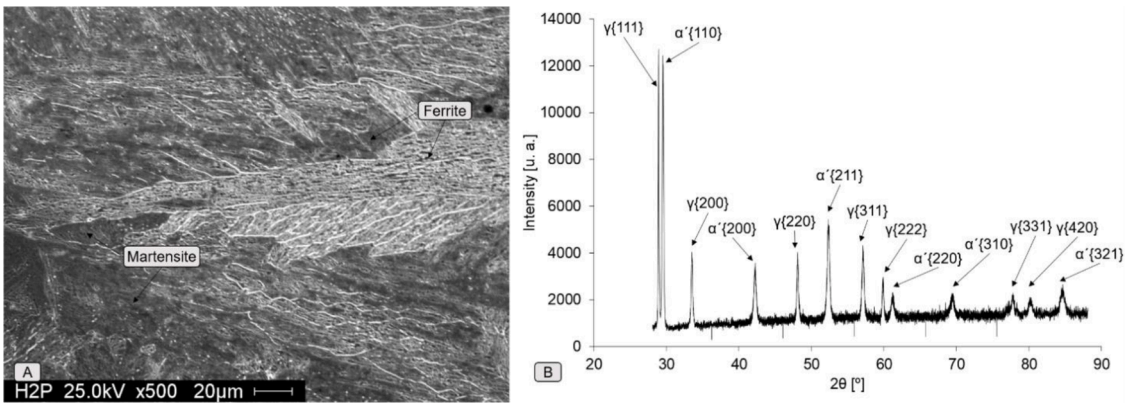

Fig. 8. Microstructure in tempering condition. A: *SEM*; B: *XRD* pattern showing alpha/alpha' and gamma diffraction peaks in tempering condition.

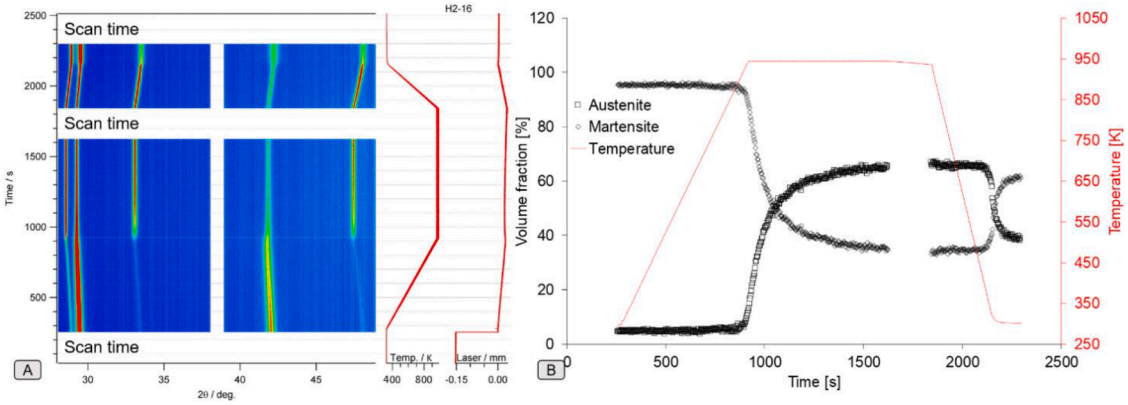

Fig. 9. A: Intensity map; B: Austenite content evolution.

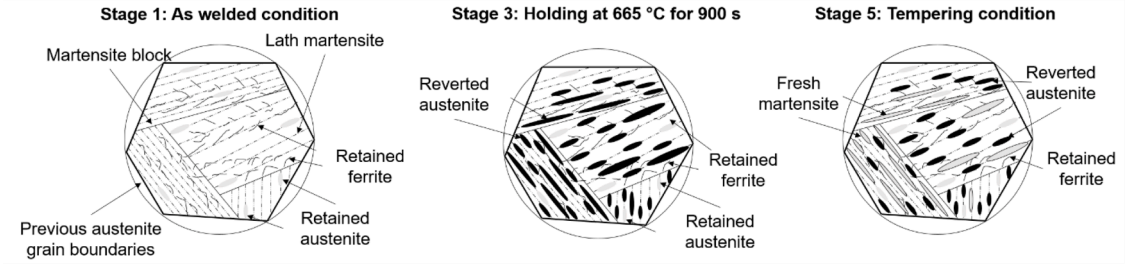

Fig. 10. Schemes of the microstructural evolution during the PWHT cycle.

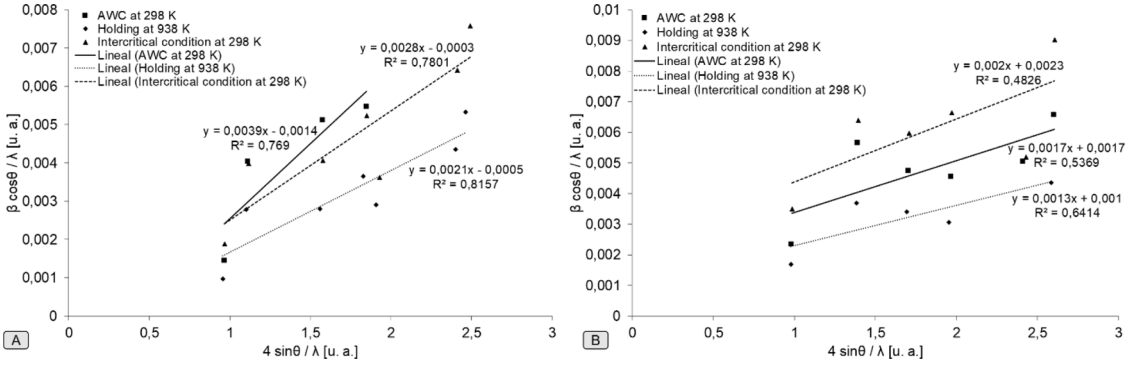

Fig. 11. Williamson-Hall method for A: austenite and B: martensite.

lattice defects.

For both martensite and austenite phases, the lattice microstrain decreased during holding up to 938 K (45.3% for austenite and 22.5% for martensite) and increased during cooling at RT. However, the lattice microstrain in the reverted austenite is higher than that in the martensite. In addition, the lattice microstrain in the martensite in the PWHT condition is higher than that in the martensite in the welded condition, indicating a greater lattice distortion. In contrast, the crystallite size of the martensite increased during heating from 590 to 1022 Angstroms and decreases during cooling until 429 Angstroms. As tempering proceeds, coherent diffraction domains (crystallites) are expected to get larger whereas the lattice distortion is expected to decrease [34].

As mentioned in the experimental procedure, it was not possible to determine the crystallite size for austenite since its intercept was negative. For a large crystallite size, the intercept should be very close to zero. As a larger crystallite size results in narrower lines, the uncertainly in the crystallite size could led to negative intercept values [35]. Thus, the negative intercept could be related to the experimental error. As the Williamson-hall method considers that both lattice microstrain and crystallite size broadening effects are independent of one another, it could be considered that the lattice microstrain was not significantly affected by the negative intercept [36,37].

Additionally, the crystallite size was determined by the Scherrer equation, for the martensite and the austenite according to Fig. 12, for the whole PWHT cycle.

The crystallite size of both phases increases with temperature during heating. In the same way, during the holding time at 938 K, the crystallite size continues growing, especially for austenite. The increase in the crystallite size could be associated to an increase in the grain size and the lattice parameter [38]. This increase is associated with the energy available (time and temperature) [34]. However, the segregation or enrichment of certain chemical elements also alter the lattice parameter. Ni would decrease the lattice parameter and hence the obtained lattice parameter should be smaller [28]. Other elements that also enrich austenite during heating, such as Cr and Mn, generate an increase in the lattice parameter. Therefore, the effects of Ni and other elements on the austenite lattice parameter, which are enriched in austenite, are overlapping. Finally, during cooling from 938 K to RT, the crystallite size decreases to its original size. For the martensite, the crystallite size estimated from both Williamson-Hall method and Scherrer equation follow a similar trend. Nevertheless, the Scherrer equation underestimated the crystallite size since it neglects the broadening caused by the lattice strain.

4. Conclusions

In-situ phase transformations of a SMSS all-weld metal were studied during the application of a post-weld heat treatment in a thermomechanical simulator with X-ray Diffraction using synchrotron radiation and dilatometry.

*Ac*1and *Ac*3showed were determined for different heating rates between 1 and 100 K/s, showing a dependence with it. The range of austenite transformation (*Ac*3 - *Ac*1) was also affected decreasing with heating rate. These aspects are relevant to the definition of PWHT temperatures and the reverted austenite formation.

The microstructure in *AW* consisted of martensitic matrix with 9% ferrite and 5% retained austenite.

For 1 K/s of heating rate, at 894 K martensite begins to transform into austenite up to the PWHT temperature (938 K), due to the existence of segregated zones, rich in gammagene elements and retained austenite from the *AW* condition. These zones act as preferential nucleation sites for the new austenite formation. Once the tempering temperature is reached and during the first 8.5 min, the martensite continues its transformation into reverted austenite in an isothermal manner, reaching a content of 71% at the end of holding stage. During cooling to RT, at

Table 5
Williamson-Hall method for martensite and austenite.

Phase	Condition	Microstrain [u. a.]	Crystallite Size [Angstroms]
Martensite	*AW* at 298 K	0.00169286	590
	Holding at 938 K	0.00131384	1022
	PWHT at 298 K	0.00204919	429
Austenite	*AW* at 298 K	0.00390318	–
	Holding at 938 K	0.00213308	–
	PWHT at 298 K	0.00284966	–

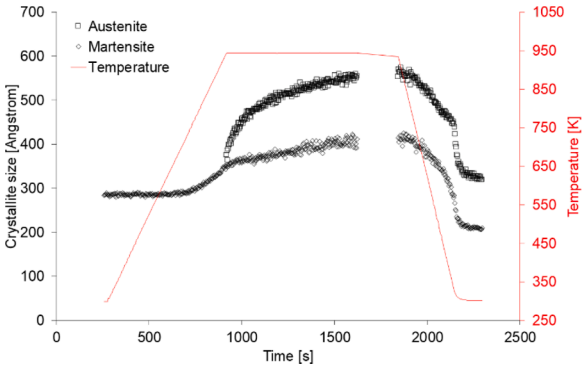

Fig. 12. Variation of crystallite size of martensite and austenite with time and temperature.

423 K, the austenite starts to transform into martensite. After intercritical PWHT, the microstructure consisted of a high content of tempered martensite (20%), retained ferrite (9%), fresh martensite (42%), and a high content of reverted austenite (29%).

Both Williamson-Hall and Scherrer equations show similar results for both phases crystallite size. There were no significant variations as a consequence of the PWHT application respect to microstrain and crystallite size, since before and after the PWHT both values are practically the same.

An initial microstructure chemically homogeneous and/or without retained austenite (without preferential nucleation sites), could affect the reverted austenite formation. This could be an interesting situation to study in a future work.

Declaration of Competing Interest

The authors declare that they have no known competing financial interests or personal relationships that could have appeared to influence the work reported in this paper.

Acknowledgments

The authors wish to thank CONARCO-ESAB for the donation of the filler metals, Air Liquide for providing the shielding gases, LNLS (Laboratório Nacional de Luz Síncrotron) for the facilities of the tests, Leonardo Wu of LNNano (Laboratório Nacional de Nanotecnologia) for the assistance, at the FI-UNLZ, UBA and INTI for financial support.

References

[1] M. Chellappan, K. Lingadurai, P. Sathiya, Characterization and optimization of TIG welded supermartensitic stainless steel using TOPSIS, in: 2017, 2017, pp. 1662–1669.
[2] Z. Sebastián, S. Estela, S. Hernán, Effects of welding procedure on corrosion resistance and hydrogen embrittlement of supermartensitic stainless steel deposits, J. Iron Steel Res. Int. 20 (12) (2013) 124–132.
[3] P.B. Srinivasan, S.W. Sharkawy, W. Dietzel, Environmental cracking behavior of submerged Arc-welded supermartensitic stainless steel weldments, J. Mater. Eng. Perform. 13 (2) (2004) 232–236.

[4] G. Pieta, et al., Evaluation of the fracture toughness of a SMSS subjected to common heat treatment cycles in an aggressive environment, J. Mater. Eng. Perform. 19 (9) (2010) 1318–1324.
[5] C.A.D. Rodrigues, et al., Effect of phosphorus content on the mechanical, microstructure and corrosion properties of supermartensitic stainless steel, Mater. Sci. Eng. A 650 (5) (2016) 75–83.
[6] Y. Lian, et al., Effect of 0.2 and 0.5% Ti on the microstructure and mechanical properties of 13Cr supermartensitic stainless steel, J. Mater. Eng. Perform. 24 (11) (2015) 4253–4259.
[7] Lippold, J.C. and B.T. Alexandrov. Phase transformation during welding and postweld heat treatment of 12Cr-6,5Ni-2,5Mo supermartensitic stainless steel. in Stainless Steel Word 2004. 2004. Netherlands.
[8] F. Niessen, N.S. Tiedje, J. Hald, Kinetics modeling of delta-ferrite formation and retainment during casting of supermartensitic stainless steel, Mater. Des. 118 (2017) 138–145.
[9] Z. De-ning, et al., Influence of tempering process on mechanical properties of 00Cr13Ni4Mo supermartensitic stainless steel, J. Iron Steel Res. Int. 17 (8) (2010) 50–54.
[10] K.G. Solheim, et al., The role of retained austenite in hydrogen embrittlement of supermartensitic stainless steel, Eng. Fail. Anal. 34 (2013) 140–149.
[11] S.Z.H. Svoboda, et al., Improving supermartensitic stainless steel weld metal toughness, Weld. J. 91 (2012) 83s–90s. March.
[12] L. Yu-rong, et al., Effect of heat treatment on microstructure and property of Cr13 super martensitic stainless steel, J. Iron Steel Res. Int. 18 (11) (2011) 60–66.
[13] S. Zappa, H. Svoboda, E. Surian, Effect of post-weld heat treatment on the mechanical properties of supermartensitic stainless steel deposit, J. Mater. Eng. Perform. 26 (2) (2017) 514–521.
[14] D. Zou, et al., Influence of heat treatment temperature on microstructure and property of 00Cr13Ni5Mo2 supermartensitic stainless steel, J. Iron Steel Res. Int. 21 (3) (2014) 364–368.
[15] J.D. Escobar, et al., Compositional analysis on the reverted austenite and tempered martensite in a Ti-stabilized supermartensitic stainless steel: segregation, partitioning and carbide precipitation, Mater. Des. 15 (2017) 95–105.
[16] S.S.M. Tavares, et al., GTAW of 12% supermartensitic stainless steel using 625 nickel alloy as filler metal, Mater. Res. 24 (5) (2021) 1–7.
[17] C. Man, et al., Beneficial effect of reversed austenite on the intergranular corrosion resistance of martensitic stainless steel, Corros. Sci. 151 (2019) 108–121.
[18] A. A5.22, Specification for Stainless Steel Electrodes for Flux Cored Arc Welding and Stainless Steel Flux Cored Rods for Gas Tungsten Arc Welding, AWS Standards, American Welding Society, 2012.
[19] Cullity, B.D. and S.R. Stock, Elements of X ray diffraction. 3rd Edition ed. 2001.
[20] I.V. Ivanov, et al., Rearrangements of dislocations during continuous heating of deformed β-TiNb alloy observed by *in-situ* synchrotron X-ray diffraction, Mater. Charact. 166 (2020), 110403.
[21] G.K. Williamson, W.H. Hall, X-ray line broadening from filed aluminium and wolfram, Acta Metall. 1 (1953) 22–31.
[22] S. Lanfredi, et al., Structural characterization and Curie temperature determination of a sodium strontium niobate ferroelectric nanostructured powder, J. Solid State Chem. 184 (2011) 990–1000.
[23] Gooch, T.G., P. Woollin, and A.G. Haynes, Welding metallurgy of low carbon 13% chromium martensitic steel, in Supermartensitic Stainless Steel '99, B.W. Institute, Editor. 1999: Belgian. p. 188–195.
[24] W. Wu, et al., The relationship between alloying elements and retained austenite in martensitic stainless steel welds, Scr. Mater. 42 (2000) 1071–1076.
[25] F. Niessen, et al., Kinetics analysis of two-stage austenitization in supermartensitic stainless steel, Mater. Des. 116 (2017) 8–15.
[26] J. Sietsma, A. Bojack, L. Zhao, P.F. Morris, Austenite formation from martensite in a 13Cr6Ni2Mo supermartensitic stainless steel, Metall. Mater. Trans. A 47A (2016) 1996–2009.
[27] J.V.R. Marín, IDENTIFICACIÓN Y CUANTIFICACIÓN DE FASES EN ACERO INOXIDABLE ASTM A743 GRADO CA6NM MEDIANTE LA TÉCNICA DE DIFRACCIÓN DE RAYOS X, in FACULTAD DE MINAS - ESCUELA DE INGENIERÍA DE MATERIALES, UNIVERSIDAD NACIONAL DE COLOMBIA, Medellín, Colombia, 2009, p. 66.
[28] A. Bojack, et al., *In-situ* determination of austenite and martensite formation in 13Cr6Ni2Mo supermartensitic stainless steel, Mater. Charact. 71 (2012) 77–86.
[29] C.A.D. Rodrigues, et al., The influence of Ni content on the weldability, mechanical, and pitting corrosion properties of a high-nickel-bearing supermartensitic stainless steel, J. Mater. Eng. Perform. 30 (4) (2021) 3044–3053.
[30] F. Niessen, et al., Formation and stabilization of reversed austenite in supermartensitic stainless steel, in: Proceedings of the 24th International Federation for Heat Treatment and Surface Engineering Congress, Nice, France, 2017.
[31] J.D. Escobar, et al., Austenite reversion kinetics and stability during tempering of a Tistabilized supermartensitic stainless steel: correlative in situ synchrotron x-ray diffraction and dilatometry, Acta Mater. 138 (2017) 92–99.
[32] F. Niessen, et al., *In-situ* analysis of redistribution of carbon and nitrogen during tempering of low interstitial martensitic stainless steel, Scr. Mater. 154 (2018) 216–219.
[33] J.D. Escobar, et al., Meta-equilibrium transition microstructure for maximum austenite stability and minimum hardness in a Ti-stabilized supermartensitic stainless steel, Mater. Des. 156 (2018) 609–621.
[34] I.R.S. Filho, et al., Austenite reversion in AISI 201 austenitic stainless steel evaluated via in situ synchrotron X-ray diffraction during slow continuous annealing, Mater. Sci. Eng. A 755 (2019) 267–277.
[35] S.A. Howard, R.L. Snyder, The use of direct convolution products in profile and pattern fitting algorithms, J. Appl. Crystallogr. 22 (1989) 238–243.
[36] Y. Wu, et al., Effects of pre-deformation on precipitation behaviors and properties in Cu-Ni-Si-Cr alloy, Mater. Sci. Eng. A 742 (10) (2019) 501–507.
[37] S.V. Navas, et al., In situ analysis of cryogenic strain in silver using synchrotron radiation, Cryogenics 120 (2021), 103384.
[38] T. Ungár, et al., Correlation between subgrains and coherently scattering domains, Powder Diffr. 20 (4) (2005) 336–375.